Investigation of acoustic windows for photoacoustic imaging of intracranial blood vessels

Michelle T. Graham*, Francis X. Creighton†, and Muyinatu A. Lediju Bell*‡§
*Department of Electrical and Computer Engineering, Johns Hopkins University, Baltimore, MD
†Department of Otolaryngology - Head and Neck Surgery, Johns Hopkins Medicine, Baltimore, MD
‡Department of Biomedical Engineering, Johns Hopkins University, Baltimore, MD
§Department of Computer Science, Johns Hopkins University, Baltimore, MD

***Abstract*—Real-time intraoperative guidance during the endonasal transsphenoidal approach to minimally invasive neurosurgery is often limited to endoscopy, which is suboptimal at locating underlying blood vessels to mitigate the risks and severe complications associated with accidental injury. Transcranial photoacoustic imaging is a promising technique for real-time visualization of these structures, but it is challenged by acoustic-bone interactions which degrade image quality. We are developing simulation methods that identify viable transcranial acoustic windows for intraoperative photoacoustic visualization of these underlying structures. In our previous work on this topic, simulation models were limited to an empty cadaver skull and the eyes of an intact cadaver head, while experiments with the same intact cadaver head were limited to the ocular acoustic window. In this paper, we present our advances to the simulation methodology, including quantitative assessments of images generated from simulated data and *in silico* investigations of additional acoustic windows with the intact cadaver head model. In addition, experimental images obtained with the ocular acoustic window of the cadaver head were compared to corresponding simulation results. With experimental and simulation similarity confirmed (i.e., point spread function area difference of 5.68 mm^2), simulations were extended to explore the temple and sphenoid sinus acoustic windows. This exploration indicated that the sphenoid sinus and ocular acoustic windows provide images with the best target visibility (e.g., a generalized contrast to-noise ratio of 1.00 $\pm$ 0.00) and resolution. Considering that current transducer technology has limited ability to navigate to and within the sphenoid sinus, we conclude that the ocular cavity is the most feasible transducer location at this time.**

I. INTRODUCTION

Endoscopic transsphenoidal surgery is a minimally invasive technique in which instruments are inserted through the nasal cavities to remove pituitary tumors [1]. Critical structures, such as the internal carotid arteries (ICAs) located within 0-10 mm of the surgical site, are susceptible to iatrogenic injury leading to surgical complications, including stroke, hemorrhage, and death [2]. Although current intraoperative guidance techniques, such as stereotactic guidance and endoscopy, enable monitoring of the ICAs, they suffer from two primary limitations. First, stereotactic guidance is subject to registration errors which can become increasingly large as patient anatomy is disrupted during surgery and as the anatomy significantly deviates from that shown in preoperative x-ray computed tomography (CT) or magnetic resonance (MR) images. Second, endoscopy is unable to identify critical structures underlying bone or other tissues in the operative path [3].

Transcranial photoacoustic imaging is being explored as a promising intraoperative imaging technique for real-time visualization of the ICAs to address these well-known limitations [4]–[10]. This technique is implemented by inserting an optical source into the nasal cavity to excite the hemoglobin in blood vessels. The absorbed optical energy is then converted to acoustic energy, and an externally placed ultrasound transducer receives the resulting signals [11]. Transcranial photoacoustic imaging is challenged by the aberration, attenuation, and reverberation of acoustic waves, which combine to degrade image quality. These adverse effects are primarily caused by the heterogeneity of cranial bone and the acoustic impedance mismatch between bone and cranial tissues [12]–[14].

To address these challenges, we previously developed a simulation framework to identify naturally occurring acoustic windows in the adult human skull for transcranial visualization of the ICAs [15]. Photoacoustic simulations were demonstrated as a promising, patient-specific tool for preoperative planning of photoacoustic image-guided neurosurgeries, based on an empty skull simulation model and individual acoustic sensor measurements (i.e., maximum pressure and signal energy). This paper advances our previous simulations by using a CT volume based on an intact cadaver head model and by comparing experimental and simulated photoacoustic images.

II. MATERIALS AND METHODS

Three-dimensional photoacoustic simulations were performed using the k-Wave toolbox [16], [17], based on the CT volume of a human cadaver head. The CT volume was converted to heterogeneous density, speed of sound, and absorption coefficient volumes. Fig. 1 shows an axial slice of the heterogeneous speed of sound volume. To provide baseline images without the negative of effects tissue heterogeneity (i.e., aberration, attenuation, and reverberation), homogeneous volumes were modeled as the average density, speed of sound, and absorption values of the cadaver brain tissue alone. The computational grid was defined with a symmetric voxel size of 0.3 mm x 0.3 mm x 0.3 mm. Acoustic wave propagation was simulated with a time increment of 1.23^{-8} seconds. No shear waves were included in these simulations.

978-1-7281-5448-0/20/$31.00 ©2020 IEEE

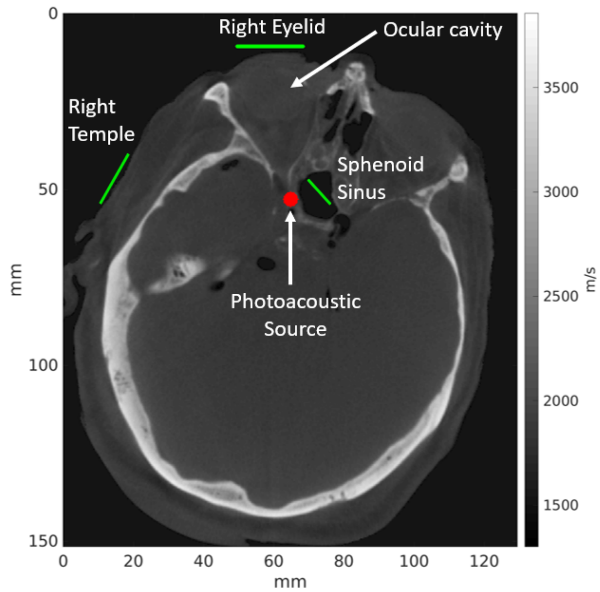

Fig. 1: Annotated axial slice of the heterogeneous speed of sound volume for k-Wave simulations, derived from a corresponding axial CT slice of a human cadaver head. A photoacoustic source was placed within the right internal carotid artery. The green lines denote transducers (i.e., photoacoustic sensors) placed on the right eyelid, on the right temple, and within the sphenoid sinus at source-to-sensor distances of 61.0 mm, 72.4 mm, and 10.3 mm, respectively.

Phased array ultrasound transducers were positioned to receive intracranial photoacoustic signals from three acoustic windows, as shown in Fig. 1. Transducers with 0.3 mm pitch, 13.5 mm height, 0 mm kerf, and 64 elements were positioned on the right eyelid and right temple region. Due to anatomical space constraints, a smaller transducer with 7.5 mm height, and 31 elements was positioned in the sphenoid sinus.

Spherical photoacoustic targets were positioned in the location of the right internal carotid artery (RCA), as shown in Fig. 1. The distances from source to the center of transducers located on the eyelid, on the temple, and within the sphenoid sinus were 61.0 mm, 72.4 mm, and 10.3 mm, respectively. Targets with 0.3 mm-diameter (point source) and 4 mm-diameter were simulated independently. Randomly distributed Gaussian noise was added to received transducer channel data to model the electronic noise of an imaging system. Two noise distributions were defined to obtain a channel signal-to-noise ratio (SNR) of 15 dB for signals received from the point target and 4 mm target with the temple transducer positions. These distributions were added to the channel data for the corresponding targets for the eyelid and temple transducer locations.

Photoacoustic delay-and-sum (DAS) images were generated from the channel data with additive noise. DAS image quality (i.e., resolution and target visibility) was measured for each transducer location. Specifically, resolution was assessed from images of the point target by calculating the area of the point

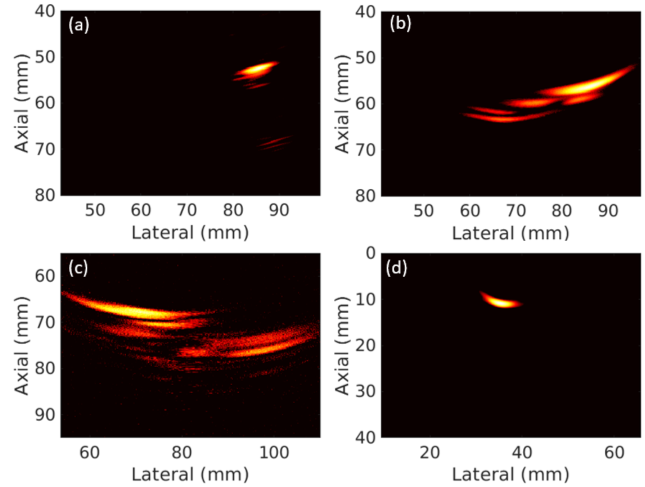

Fig. 2: (a) Experimental photoacoustic image of the right internal carotid artery obtained with the ocular acoustic window. Simulated photoacoustic images of the intracranial photoacoustic point source obtained with the (b) ocular, (c) temple, and (d) sphenoid sinus acoustic windows of the cadaver head model. Images are displayed with 15 dB dynamic range.

spread function (PSF) -6 dB contour. Target visibility was assessed from images of the the 4 mm-diameter target with contrast, SNR, contrast-to-noise ratio (CNR), and generalized contrast-to-noise ratio (gCNR) [18], [19] measurements calculated as follows:

$$\text{Contrast} = 20\log_{10}\left(\frac{\mu_t}{\mu_b}\right) \tag{1}$$

$$\text{SNR} = 20\log_{10}\left(\frac{\mu_t}{\sigma_b}\right) \tag{2}$$

$$\text{CNR} = \frac{|\mu_t - \mu_b|}{\sqrt{\sigma_t^2 + \sigma_b^2}} \tag{3}$$

$$\text{gCNR} = 1 - \sum_{k=0}^{N-1} min\{h_i(x_k), h_o(x_k)\} \tag{4}$$

where μ_t and μ_b are the means, σ_t and σ_b are the standard deviations, and h_t and h_b are the histograms of the signal amplitudes within ellipsoidal regions of interest (ROIs) inside and outside of a photoacoustic target, respectively. N is the number of bins in the histogram, and k is the index of the bin. For each image, a singular target ROI and multiple background ROIs were chosen to calculate means and standard deviations of measurements. These simulation results were validated with experimental images obtained with the ocular acoustic window of the cadaver head, using the experimental procedure and data described in our previous publication [15].

III. Results & Discussion

Figs. 2(a) and 2(b) show experimental and simulated photoacoustic images of the RCA from the human cadaver head, respectively, each obtained with the ocular acoustic window.

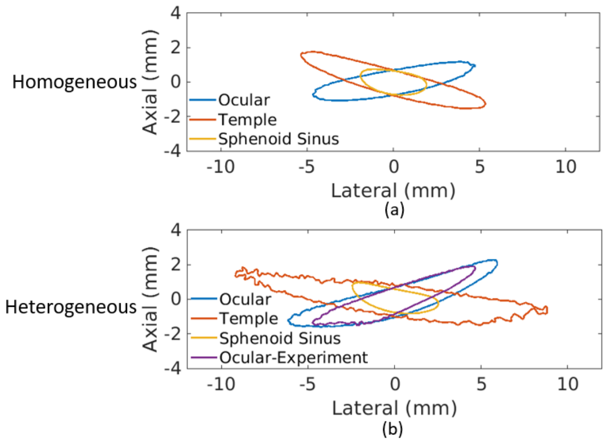

Fig. 3: Point spread function -6 dB contours for the (a) homogeneous point target simulations and (b) heterogeneous point target simulations and experimental image.

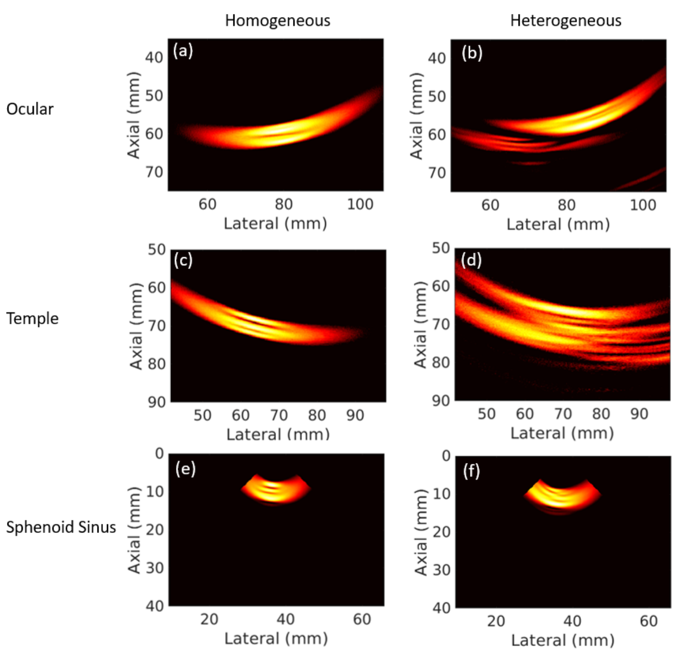

Fig. 4: Homogeneous and heterogeneous simulated photoacoustic images of the 4 mm-diameter target obtained with the (a,b) ocular, (c,d) temple, and (d,e) sphenoid sinus acoustic windows. Image are displayed with 15 dB dynamic range.

Although the simulated image shows more artifacts than the experimental image, the shape, location, and visibility of the targets generally agree. Figs. 2(c) and 2(d) show the simulated images of the point target obtained with the temple and sphenoid sinus acoustic windows, respectively. Artifacts visible in the image obtained with the temple acoustic window are absent in the image obtained with the sphenoid sinus acoustic window. The simulation results in Figs. 2(b)-2(d) indicate that the sphenoid sinus is the preferable transducer location due to this location producing the least artifacts in simulation.

Fig. 3 shows the -6 dB contours of the experimental and simulated photoacoustic point target images. To provide baseline measurements, the contour areas of the homogeneous simulated images were 10.82 mm^2, 12.80 mm^2, and 4.22 mm^2 for the ocular, temple, and sphenoid sinus acoustic windows, respectively. The areas of the corresponding simulated images obtained with the cadaver head model and displayed in Figs. 2(b-d) were 16.26 mm^2, 23.34 mm^2, and 5.44 mm^2, respectively. We observed the smallest impact on resolution from heterogeneous tissues in the acoustic pathway with the sphenoid sinus acoustic window. Therefore, the sphenoid sinus transducer location provides images with the best resolution, likely due to minimal bone present in the acoustic pathway and shallow target imaging depth. In addition, the corresponding area of the ocular experimental image was 10.59 mm^2, which indicates good agreement between this experimental result and the heterogeneous ocular simulation, as observed in Fig. 3(b).

Fig. 4 shows photoacoustic images generated from homogeneous and heterogeneous simulations of a 4 mm-diameter target to assess target visibility. In each homogeneous simulated image, the clearly visible target provides a baseline to assess target visibility. The presence of brain, bone, and skin tissues causes differences between the homogeneous baseline (Figs. 4(a,c,e)) and heterogeneous images (Figs. 4(b,d,f)). Qualitatively, the heterogeneous image obtained with the temporal acoustic window shows prominent artifacts near the target, which negatively affect target visibility. Although the heterogeneous image obtained with the ocular acoustic window also shows artifacts, these artifacts are distinct from the target and do not negatively affect the target visibility. Therefore, the ocular location is a more feasible transducer position than the temporal region. The homogeneous and heterogeneous images obtained with the sphenoid sinus acoustic window display a similar target appearance, without visible artifacts in the heterogeneous image, which suggests that the sphenoid sinus transducer location is most optimal. However, miniaturized endonasal transducers for navigation to and within the sphenoid sinus are not readily available. Based on these results, we propose the ocular acoustic window when the sphenoid sinus window is logistically infeasible, which agrees with the conclusions of our previous publication [15].

Fig. 5 quantifies the target visibility of the heterogeneous simulated images displayed in Fig. 4. Images obtained with the sphenoid sinus acoustic window produced contrast, SNR, CNR, and gCNR measurements of 23.02 $\pm$ 3.48 dB, 35.15 $\pm$ 4.30 dB, 6.04 $\pm$ 0.22, and 1.00 $\pm$ 0.00, respectively. These measurements generally outperformed measurements obtained with the ocular and temporal acoustic windows. When the sphenoid sinus transducer location is logistically infeasible, the ocular acoustic window provides suitable target visibility, and notably identical gCNR, which is arguably the most important indicator of a surgeon's ability to visualize a target [19]. Considering that the sphenoid sinus location provides images with the best target visibility and resolution, these results provide additional motivation for the development of dedicated nasal intraoperative transducers for transcranial photoacoustic

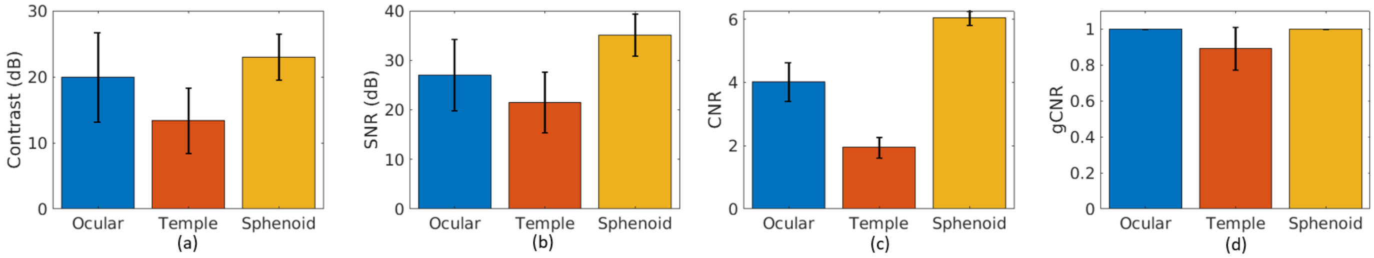

Fig. 5: Mean ± one standard deviation of (a) contrast, (b) signal-to-noise ratio (SNR), (c) contrast-to-noise ratio (CNR), and (d) generalized contrast-to-noise ratio (gCNR) measurements from the heterogeneous simulated photoacoustic images of the 4 mm-diameter target. Singular target and multiple background ROIs were used to calculate the mean and standard deviation.

imaging [15], [20].

IV. Conclusion

The work presented in this paper details advances in our patient-specific simulation methodology for presurgical planning of transducer placement for intraoperative photoacoustic image guidance. Although the sphenoid sinus was identified as an optimal acoustic window for photoacoustic visualization of the ICAs (based on resolution and target visibility measurements), this window is logistically infeasible with current transducer technology. Therefore, the ocular cavity was identified as the next best acoustic window option when considering both ICA visibility and logistical feasibility (despite the reduced resolution). These simulation results additionally motivate the development of intraoperative transducers that exploit the sphenoid sinus acoustic window for transcranial photoacoustic visualization of the ICAs.

Acknowledgments

This research is supported by NIH R00-EB018994, NSF CAREER Award ECCS 1751522, and NSF Graduate Research Fellowship DGE 1746891.

References

[1] P. Cappabianca, L. M. Cavallo, and E. de Divitiis, "Endoscopic endonasal transsphenoidal surgery," *Neurosurgery*, vol. 55, pp. 933–941, 2004.

[2] M. S. Agam, M. A. Wedemeyer, B. Wrobel, M. H. Weiss, J. D. Carmichael, and G. Zada, "Complications associated with microscopic and endoscopic transsphenoidal pituitary surgery: experience of 1153 consecutive cases treated at a single tertiary care pituitary center," *Journal of Neurosurgery*, vol. 130, no. 5, pp. 1576–1583, 2018.

[3] K. Kitazawa, H. Okudera, T. Takemae, and S. Kobayashi, "CT guided transsphenoidal surgery: report of nine cases," *Neurological Surgery*, vol. 21, no. 147, 1993.

[4] X. Wang, D. L. Chamberland, and G. Xi, "Noninvasive reflection mode photoacoustic imaging through infant skull toward imaging of neonatal brains," *Journal of Neuroscience Methods*, vol. 168, no. 2, pp. 412 – 421, 2008.

[5] M. A. L. Bell, A. K.Ostrowski, K. Li, P. Kazanzides, and E. M. Bocto, "Localization of transcranial targets for photoacoustic-guided endonasal surgeries," *Photoacoustics*, vol. 3, no. 2, pp. 78–87, 2015.

[6] M. A. L. Bell, A. K. Ostrowski, K. Li, P. Kazanzides, and E. Boctor, "Quantifying bone thickness, light transmission, and contrast interrelationships in transcranial photoacoustic imaging," in *Proc. SPIE, Photons Plus Ultrasound: Imaging and Sensing*, vol. 9323, 2015.

[7] M. A. L. Bell, A. B. Dagle, P. Kazanzides, and E. M. Boctor, "Experimental assessment of energy requirements and tool tip visibility for photoacoustic-guided endonasal surgery," in *Proc. SPIE, Photons Plus Ultrasound: Imaging and Sensing*, vol. 9708, 2016, p. 97080D.

[8] M. A. L. Bell, A. K. Ostrowski, P. Kazanzides, and B. Emad, "Feasibility of transcranial photoacoustic imaging for interventional guidance of endonasal surgeries," in *Proc. SPIE, Photons Plus Ultrasound: Imaging and Sensing*, vol. 8943, no. 894307, 2014.

[9] T. Kirchner, J. Gröhl, N. Holzwarth, M. A. Herrera, A. Hernández-Aguilera, E. Santos, and L. Maier-Hein, "Photoacoustic monitoring of blood oxygenation during neurosurgical interventions," in *Proc. SPIE, Photons Plus Ultrasound: Imaging and Sensing*, vol. 10878, 2019, pp. 14 – 18.

[10] M. F. Kircher, A. De La Zerda, J. V. Jokerst, C. L. Zavaleta, P. J. Kempen, E. Mittra, K. Pitter, R. Huang, C. Campos, F. Habte *et al.*, "A brain tumor molecular imaging strategy using a new triple-modality mri-photoacoustic-raman nanoparticle," *Nature Medicine*, vol. 18, no. 5, pp. 829–834, 2012.

[11] P. Beard, "Biomedical photoacoustic imaging," *Interface Focus*, vol. 1, no. 4, pp. 602–631, 2011.

[12] M. Kneipp, J. Turner, H. Estrada, J. Rebling, S. Shoham, and D. Razansky, "Effects of the murine skull in optoacoustic brain microscopy," *Journal of Biophotonics*, vol. 9, no. 1-2, pp. 117–123, 2016.

[13] G. Pinton, J.-F. Aubry, E. Bossy, M. Muller, M. Pernot, and M. Tanter, "Attenuation, scattering, and absorption of ultrasound in the skull bone," *Medical Physics*, vol. 39, no. 1, pp. 299–307, 2012.

[14] H. Estrada, J. Rebling, J. Turner, and D. Razansky, "Broadband acoustic properties of a murine skull," *Physics in Medicine & Biology*, vol. 61, no. 5, p. 1932, 2016.

[15] M. T. Graham, J. Huang, F. Creighton, and M. A. L. Bell, "Simulations and human cadaver head studies to identify optimal acoustic receiver locations for minimally invasive photoacoustic-guided neurosurgery," *Photoacoustics*, p. 100183, 2020.

[16] B. E. Treeby and B. T. Cox, "k-Wave: MATLAB toolbox for the simulation and reconstruction of photoacoustic wave fields," *Journal of Biomedical Optics*, vol. 15, no. 2, p. 021314, 2010.

[17] B. E. Treeby, B. T. Cox, and J. Jaros, *A MATLAB toolbox for the time domain simulation of acoustic wave field, User manual, (2016) Manual Version 1.1, Toolbox Release 1.1*.

[18] A. Rodriguez-Molares, O. M. H. Rindal, J. D'hooge, S.-E. Måsøy, A. Austeng, M. A. L. Bell, and H. Torp, "The generalized contrast-to-noise ratio: a formal definition for lesion detectability," *IEEE Transactions on Ultrasonics, Ferroelectrics, and Frequency Control*, vol. 67, no. 4, pp. 745–759, 2019.

[19] K. M. Kempski, M. T. Graham, M. R. Gubbi, T. Palmer, and M. A. L. Bell, "Application of the generalized contrast-to-noise ratio to assess photoacoustic image quality," *Biomedical Optics Express*, vol. 11, no. 7, pp. 3684–3698, 2020.

[20] M. A. Lediju Bell, "Photoacoustic imaging for surgical guidance: Principles, applications, and outlook," *Journal of Applied Physics*, vol. 128, no. 6, p. 060904, 2020.